ARTICLES

Multiple Explosion Pathways of the Deuterated Benzene Trication in 9-fs Intense Laser Fields

Akitaka Matsuda,[†] Mizuho Fushitani,[†,‡] Richard D. Thomas,[§] Vitali Zhaunerchyk,[§] and Akiyoshi Hishikawa*[,†,‡,∥]

Institute for Molecular Science, National Institutes of Natural Sciences, Myodaiji, Okazaki, Aichi 444-8585, Japan, The Graduate University for Advanced Studies (SOKENDAI), Myodaiji, Okazaki, Aichi 444-8585, Japan, Department of Physics, Albanova University Centre, Stockholm University, SE-106 91 Stockholm, Sweden, and PRESTO, Japan Science and Technology Agency, Kawaguchi, Saitama 332-0012, Japan

Received: July 22, 2008; Revised Manuscript Received: October 8, 2008

The fragmentation of deuterated benzene (C_6D_6) in ultrashort intense laser fields (9 fs, 1×10^{15} W/cm^2) is studied by the ion-coincidence momentum imaging technique. Five two-body and eight three-body Coulomb explosion pathways from the trication ($C_6D_6^{3+}$), associated with the deprotonation and ring-opening reactions, are identified. It is found from the fragment momentum correlation that all the observed three-body explosion processes proceed sequentially via the two-body Coulomb explosion forming molecular dications, $C_mD_n^{2+}$, with $(m,n) = (6,5)$, (5,5), (5,4), (4,4), (4,3), and (3,3), which further dissociate into pairs of monocations. The branching ratio of the fragmentation pathways estimated from the number of the observed coincidence events indicates that the fragmentation is nonstatistical.

I. Introduction

The formation and fragmentation of multiply charged molecular ions are commonly observed as the responses of molecules exposed to intense laser fields. The fragmentation dynamics in these interactions have been extensively studied in recent years[1,2] as they provide insight into the interplay between the electron and nuclear dynamics with large degrees of nuclear freedom in the presence of strong alternating electric fields. Benzene and other aromatic molecules in intense laser fields have especially attracted a number of experimental[3−12] and theoretical studies.[13−15] The time-of-flight mass spectra of benzene in femtosecond intense laser fields (∼100 fs, 800 nm) recorded at relatively weak intensity (∼10^{13} W/cm^2) shows that the singly charged parent ion, $C_6H_6^+$, is the dominant product.[3] On the other hand, a variety of molecular fragment ions, such as $C_3H_m^+$ ($m = 0-3$) and $C_2H_n^+$ ($n = 0-4$), start to appear at field intensities of ∼10^{14} W/cm^2,[4,5,8,9,16,17] while the formation of atomic fragment ions, C^+ and H^+, is observed at even higher field intensities (>10^{15} W/cm^2).[6,7]

The experimental studies reported so far on the response of benzene in intense laser fields have been based on the mass spectrometry of the fragment ions. The peaks of the individual fragment ions in the mass spectra, however, are built up of contributions which come from the different fragmentation pathways from the various charge states of the parent ion produced in the laser field, thus hampering detailed discussion on the fragmentation dynamics. Here we employ the coincidence momentum imaging technique[18] to clarify the fragmentation process of benzene in intense laser fields (1×10^{15} W/cm^2). By use of this technique we can unambiguously identify the Coulomb explosion pathways from one particular charge state of interest and determine the momenta of the fragment ions in the laboratory frame. As a first step to understand the dynamics of benzene in intense laser fields, we employ a few cycle laser pulses with a duration of 9 fs to clarify the dissociation dynamics in the benzene trication. The ultrashort laser pulses suppress the nuclear dynamics during the interaction with the laser fields so that we can give a detailed comparison with the previous studies[13−15,19,20] on the field-free dissociation of highly charged benzene, which elucidates the characteristic nature of ionization process in intense laser fields. In the present study we focus on the two- and three-body Coulomb explosion pathways from the benzene trication. The fragmentation dynamics are discussed based on the momentum correlation of the three fragment ions as they provide a deeper understanding on the molecular structural deformation[18] and the bond breaking dynamics.[21]

II. Experimental Section

The experimental setup has been described previously[22,23] and so will only be briefly discussed here. The ultrashort laser pulses were generated by a pulse compressor consisting of a hollow fiber and a pair of dispersive mirrors. The output of a Ti:sapphire laser amplifier system (35 fs, 800 nm, 1 kHz) was coupled by a lens ($f = 1200$ mm) into a 800-mm-long hollow fiber (core diameter 500 μm) placed in an Ar cell (0.07 MPa). The fiber output was then collimated by a concave silver mirror and recompressed with several reflections on broadband dispersive mirrors to generate few-cycle laser pulses in the sub-10 fs regime. The linearly polarized laser pulse was introduced into a ultrahigh vacuum chamber (<10^{-8} Pa) and focused by a

* To whom correspondence should be addressed. Phone: +81-564-55-7419. Fax: +81-564-55-7391. E-mail: hishi@ims.ac.jp.
[†] Institute for Molecular Science.
[‡] The Graduate University for Advanced Studies.
[§] Stockholm University.
[∥] Japan Science and Technology Agency.

10.1021/jp806466x CCC: $40.75
Published on Web 02/16/2009

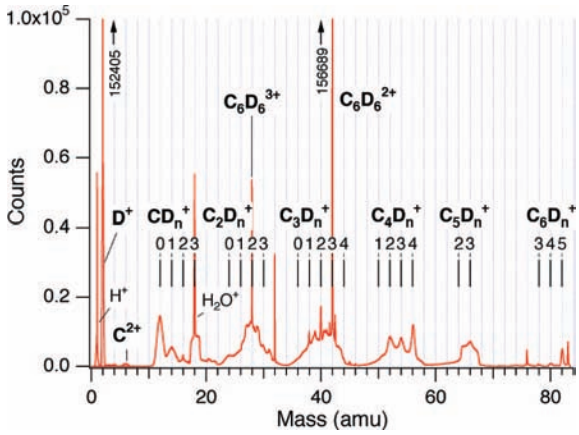

Figure 1. Time-of-flight mass spectra of deuterated benzene C_6D_6 in 9-fs intense laser fields (1×10^{15} W/cm^2) obtained for 3×10^7 laser shots.

concave mirror ($f = 75$ mm) placed in the chamber to generate ultrashort intense laser fields.

The pulse duration was measured by interferometric autocorrelation using a high-precision Michelson interferometer placed between the hollow fiber and the dispersive mirrors. The autocorrelation trace was recorded as the second harmonic signal from a thin BBO crystal placed behind the entrance window used for the vacuum chamber. To obtain ultrashort (9 fs) laser pulses at the focal spot, dispersion introduced by optical materials such as the vacuum chamber window was precompensated for by optimizing the number of the reflections on the dispersive mirrors. After the pulses were characterized, one of the arms of the Michelson interferometer was blocked to allow the coincidence measurements to be performed with single laser pulses.

In order to obtain sufficient mass separation of the fragment ions and to avoid significant contamination from the residual H_2O in the vacuum chamber, deuterated benzene (C_6D_6) was used and introduced as a skimmed effusive beam into the interaction region. All the fragment ions produced by the Coulomb explosion processes studied here were guided with a 4π collection efficiency to a fast position sensitive detector (Roentdek HEX80), by extraction parallel-plate electrodes in a velocity mapping configuration.[24] The ions were accelerated by the static electronic field in front of the detector up to 4 keV, which is high enough to saturate the detection efficiency of the microchannel plates (~0.6, determined by the aperture ratio), almost independently of ion species.[25,26] The momenta of the respective ions in the molecular frame, $\mathbf{p}_i = (p_x^i, p_y^i, p_z^i)$ ($i = 1, 2,...$), are determined from the (x, y) position and the time-of-flight t at the arrival at the detector[18,22,27] for every single event of the Coulomb explosion process.

The data acquisition was performed in the common stop mode. The stop trigger pulse was set to prevent the detection of the parent $C_6D_6^+$ ion (see Figure 1). The total kinetic energy release E_{kin} was calculated from the measured momenta, $E_{kin} = \Sigma\, p_i^2/(2m_i)$, where m_i and p_i are the mass and the absolute value of the momentum for the ith fragment ion ($p_i = |\mathbf{p}_i|$), respectively.

III. Results and Discussion

A. Time-of-Flight Mass Spectra (TOFMS). Figure 1 shows the TOFMS of fragment ions produced from the fragmentation of C_6D_6 in 9-fs intense laser fields (1×10^{15} W/cm^2) recorded with 3×10^7 laser shots. As observed previously,[4,7,8] the highly charged parent ions, $C_6D_6^{2+}$ and $C_6D_6^{3+}$, are especially prominent

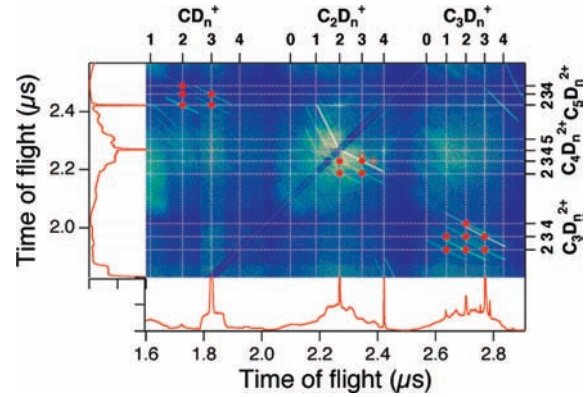

Figure 2. Double coincidence map obtained for deuterated benzene C_6D_6 in 9-fs intense laser fields (1×10^{15} W/cm^2), shown with corresponding TOFMS. The sharp lines (with slopes with -2 or $-1/2$) in the map marked with solid circles indicates the pair formation of singly charged and doubly charged fragment ions. In addition to five two-body Coulomb explosion pathways (see Table 1), ten different neutral pathways such as $C_6D_6^{3+} \rightarrow C_2D_2^+ + C_4D_3^{2+} + D$, are identified. Features associated with ^{13}C are marked with open circles.

TABLE 1: Two-Body Coulomb Explosion Pathways of C_6D_6 in 9-fs Intense Laser Fields (1×10^{15} W/cm^2) Identified by the Double Ion-Coincidence Momentum Imaging Technique

parent	pathway		N_{coinc}[a]	β	E_{kin}[b] (eV)
$C_6D_6^{3+} \rightarrow$	$CD_2^+ + C_5D_4^{2+}$	2a	258(16)	0.4(1)	7.0(1)
	$CD_3^+ + C_5D_3^{2+}$	2b	1054(32)	0.1(1)	6.8(1)
	$C_2D_3^+ + C_4D_3^{2+}$	2c	13795(117)	0.1(1)	6.4(1)
	$C_3D_2^+ + C_3D_4^{2+}$	2d	2109(45)	0.3(1)	6.3(1)
	$C_3D_3^+ + C_3D_3^{2+}$	2e	8719(93)	−0.1(2)	5.9(1)

[a] Obtained with 3×10^7 laser shots and the momentum conservation condition, $|\Sigma_i \mathbf{p}_i| \leq 8.3$ au. The experimental uncertainty is estimated as $\sqrt{N_{coinc}}$. [b] Peak value.

in the spectra, with high peak counts of ~1.5×10^5 and 5×10^4, respectively. In addition, the singly charged fragment ions, D^+, CD_n^+ ($n = 0-3$), $C_2D_n^+$ ($n = 0-3$), $C_3D_n^+$ ($n = 0-4$), $C_4D_n^+$ ($n = 1-4$), $C_5D_n^+$ ($n = 2,3$), $C_6D_n^+$ ($n = 3-5$), are clearly observed. The doubly charged fragment molecular ions,[8] $C_3D_n^{2+}$ ($n = 2-4$), $C_4D_n^{2+}$ ($n = 2,3$) and $C_5D_n^{2+}$ ($n = 2-4$), are not clearly visible in the TOF spectrum, but are readily identified in the double coincidence map in Figure 2 as described later. Although the peak intensities of these singly and doubly charged fragment ions are small, the total sum of counts due to the fragment ions in the integrated spectrum area is substantially larger than those of the highly charged parent ions, showing that the fragmentation is the major pathway under the present experimental conditions.

B. Coulomb Explosion Pathways of Benzene Trication, $C_6D_6^{3+}$. To understand the fragmentation dynamics of the benzene trication ($C_6D_6^{3+}$) formed in 9-fs intense laser fields (1×10^{15} W/cm^2), we examined all of the possible two-body and three-body Coulomb explosion pathways arising from the combinations of the observed fragment ions listed earlier. The two-body pathways from $C_6D_6^{3+}$ are clearly identified as sharp straight lines with slopes of -2 or $-1/2$ in the double coincidence map in Figure 2. The pathways thus identified in the present study are listed in Table 1 and Table 2 for the two-body and three-body explosion processes, respectively. For the two-body fragmentation, all of the pathways originate from the ring-opening reaction, where the fragmentation through the pathways 2c and 2e contributes more than 80% of the total two-body explosion process. Ring-opening also dominates in the three-body Coulomb explosion process, accompanying (i) the ejection

TABLE 2: Three-Body Coulomb Explosion Pathways of C_6D_6 in 9-fs Intense Laser Fields (1×10^{15} W/cm^2) Identified by the Triple Ion-Coincidence Momentum Imaging Technique

parent	pathway		N_{coinc}[a]	E_{kin}[b] (eV)
$C_6D_6^{3+} \rightarrow$	$D^+ + C_2D_2^+ + C_4D_3^+$	3a	2212(46)	9.8(2)
	$D^+ + C_2D_3^+ + C_4D_2^+$	3b	1952(40)	9.8(2)
	$D^+ + C_3D_2^+ + C_3D_3^+$	3c	3743(61)	9.8(2)
	$CD^+ + C_2D_2^+ + C_3D_3^+$	3d	440(21)	11.5(2)
	$CD_2^+ + C_2D_2^+ + C_3D_2^+$	3e	1963(44)	11.5(2)
	$CD_2^+ + C_2D_3^+ + C_3D^+$	3f	1925(44)	10.5(2)
	$CD_3^+ + C_2D_2^+ + C_3D^+$	3g	4190(65)	11.4(2)
	$C_2D_2^+ + C_2D_2^+ + C_2D_2^+$	3h	2822(53)	12.5(3)

[a] Obtained with 3×10^7 laser shots and the momentum conservation condition, $|\sum_i \mathbf{p}_i| \leq 8.3$ au. The experimental uncertainty is estimated as $\sqrt{N_{coinc}}$. [b] Peak value.

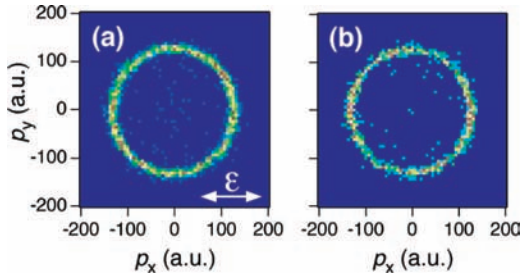

Figure 3. Coincidence ion images for the two-body Coulomb explosion pathways (a) $C_3D_3^+ + C_3D_3^{2+}$ and (b) $C_2D_3^+ + C_4D_3^{2+}$, obtained as a slice of three-dimentional momentum distribution along the $p_x p_y$ momentum plane ($|p_z| \leq 10$ au). The direction of the laser polarization vector (ε) is indicated by an arrow.

of a deuterium ion (pathways 3a−3c) or (ii) the three-body ring breakup (pathways 3d−3 h). The ejection of neutral deuterium atoms from the trication, e.g., $C_6D_6^{3+} \rightarrow C_2D_2^+ + C_4D_3^{2+} + D$, is also identified in Figure 2, which forms broader features due to the momentum imparted into the deuterium atom as discussed for the benzene dication.[19,20]

Coincidence ion images for the two-body Coulomb explosion pathways 2c and 2e are shown in Figure 3. These ion images, obtained as a slice of three-dimentional momentum distribution along the $p_x p_y$ momentum plane, exhibit isotropic distributions. The anisotropy parameters, β, obtained by the least-squares fitting to the function $I(\theta) = 1 + \beta P_2(\cos\theta)$,[28] are small ($-0.1 \leq \beta \leq 0.4$) for all of the observed two-body pathways as listed in Table 1.

The distributions of the total kinetic energy release, E_{kin}, calculated from the momenta of the corresponding fragment ion, are shown in Figure 4 for each of the fragmentation pathways. They exhibit a broad single peak at ∼6 eV for the two-body explosion pathways (see Table 1) and at ∼10−12 eV for the three-body pathways (Table 2), respectively.

The peak values of E_{kin} for the three-body Coulomb explosion from the triply charged state are smaller than those observed for smaller polyatomic molecules which undergo direct three-body explosion in sub-10 fs intense laser fields, such as H_2S (15 eV for the laser polarization vector parallel to the molecular plane and 20 eV for perpendicular)[22] and acetylene (17 eV).[29]

C. Momentum Correlation Analysis of the Three-Body Pathways. As has been discussed previously,[21,30] a three-body Coulomb explosion process, $ABC^{3+} \rightarrow A^+ + B^+ + C^+$, can be described in the fragment momentum space spanned by three independent momentum parameters. A set of the three momentum parameters can be chosen arbitrarily. Here we adopt ($p(A^+)$, $p(B^+)$, $p(C^+)$) to form just such a set of three parameters, where

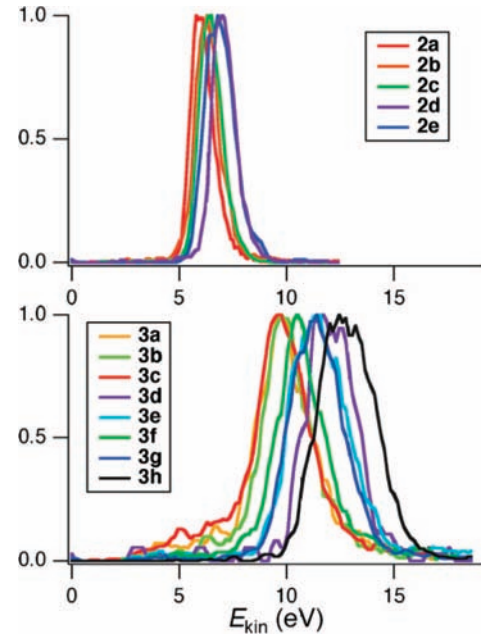

Figure 4. Distributions of the kinetic energy release E_{kin} for the two-body (upper panel) and the three-body (lower panel) explosion pathways (see Tables 1 and 2), observed for C_6D_6 in 9-fs intense laser fields (1×10^{15} W/cm^2).

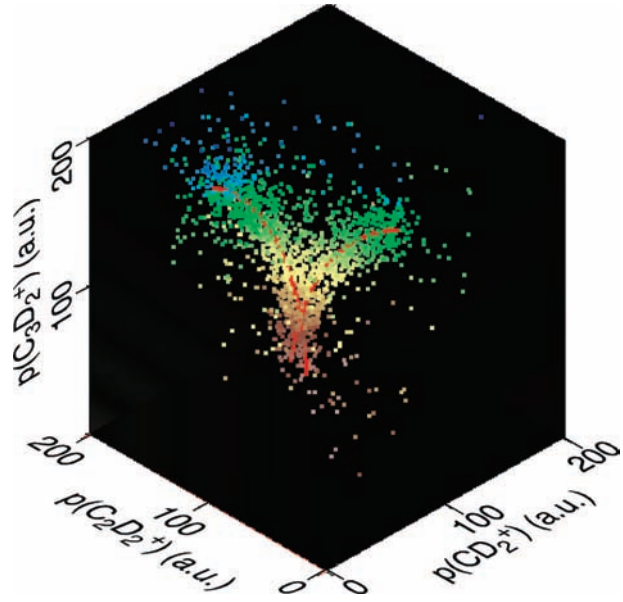

Figure 5. Three-dimensional momentum correlation map, plotting all the coincidence events identified for the three-body Coulomb explosion pathway, $C_6D_6^{3+} \rightarrow C_3D_2^+ + C_2D_2^+ + CD_2^+$. The results of simulations based on the free-rotor model for the sequential three-body explosion are shown by the red solid lines.

$p(M^+)$ is the magnitude of the momenta of the fragment ion, $p(M^+) = |\mathbf{p}(M^+)|$ (M = A, B, C).

The three-dimensional momentum plot for the three-body Coulomb explosion pathway (3e), $C_6D_6^{3+} \rightarrow CD_2^+ + C_2D_2^+ + C_3D_2^+$, is shown in Figure 5 where each dot represents a single Coulomb explosion event. The three-dimensional map shows two distinct features which form wing-like distributions. The origin of these characteristic features is elucidated in the projection of all the coincidence events onto the two-dimensional planes shown in parts c and d of Figure 6. As seen in the two-dimensional momentum correlation map in Figure 6c, the two observed wings are mapped to two straight lines along the x

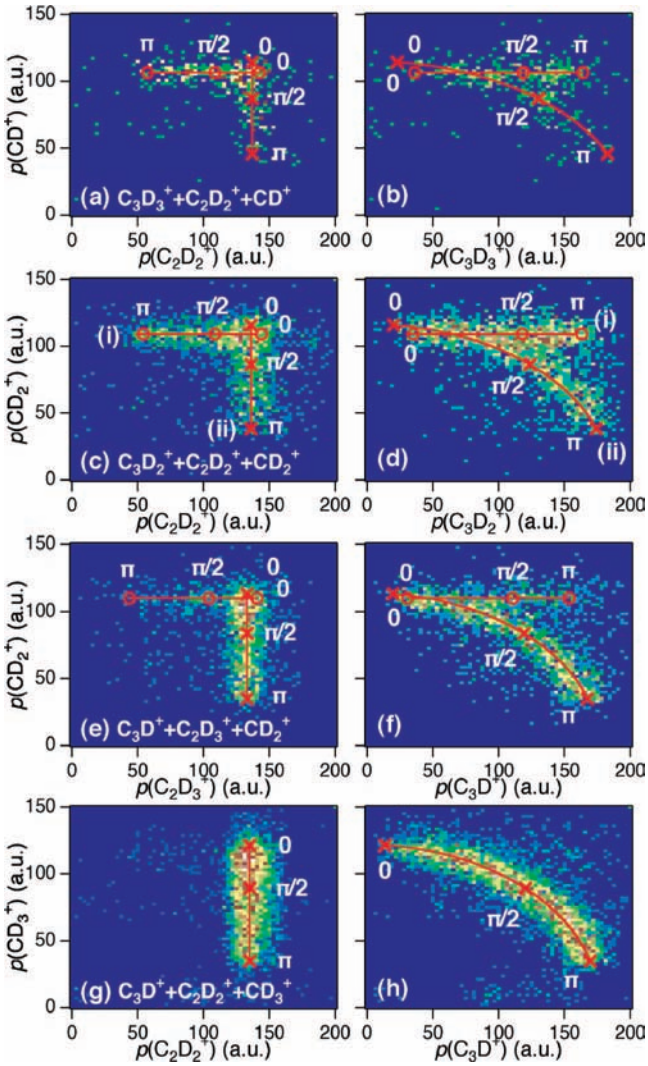

Figure 6. Two-dimensional momentum correlation maps for the three-body Coulomb explosion pathways, 3d−3g (see Table 2). The results of simulations based on the free-rotor model for the sequential three-body explosion are shown by the red solid lines. The momentum angle between $\mathbf{p}_I$ and $\mathbf{p}_{II}$ (see text) is indicated with circles or crosses on the simulated lines.

and y axes, respectively. Such distributions are characteristic of the stepwise or sequential three-body fragmentation process.[21] For example, the distribution running along the x axis (labeled as (i) in Figure 6c) indicates that the momentum value of the CD_2^+ fragment ion, $p(CD_2^+)$, is constant, while the momentum value of $C_2D_2^+$ (and that of $C_3D_2^+$) take a wide distribution of values. This means that the ejection of CD_2^+ is determined independently from the formation of $C_2D_2^+$ and $C_3D_2^+$, suggesting that the three-body explosion process proceeds as $C_6D_6^{3+} \rightarrow CD_2^+ + C_5D_4^{2+} \rightarrow CD_2^+ + C_2D_2^+ + C_3D_2^+$, i.e., via the formation of a precursor ion, $C_5D_4^{2+}$. The other wing labeled as (ii) in Figure 6c hence corresponds to the sequential process via $C_4D_4^{2+}$, i.e., $C_6D_6^{3+} \rightarrow C_2D_2^+ + C_4D_4^{2+} \rightarrow C_2D_2^+ + CD_2^+ + C_3D_2^+$.

The sequential three-body processes can be described by a simple model that has been previously presented,[21,31] in which the doubly charged precursor molecular ion rotates freely from the Coulomb interaction with the counterpart ion produced in the first step. Under this assumption, the final momenta of fragment ions formed by a sequential process, $ABC^{3+} \rightarrow A^+ + BC^{2+} \rightarrow A^+ + B^+ + C^+$, can be expressed as[21]

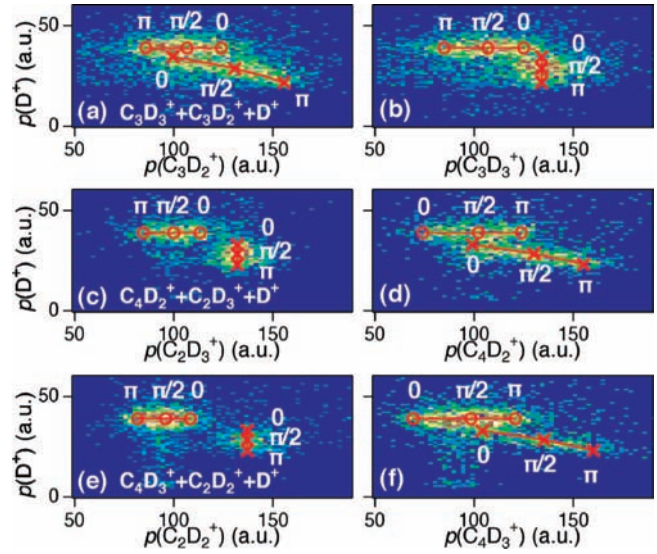

Figure 7. Two-dimensional momentum correlation maps for the three-body Coulomb explosion pathways, 3a−3c, involving the ejection of D^+ (see Table 2). The results of simulations based on the free-rotor model for the sequential three-body explosion are shown by the red solid lines. The momentum angles between $\mathbf{p}_I$ and $\mathbf{p}_{II}$ (see text) are indicated with circles or crosses on the simulated lines.

$$\mathbf{p}(A^+) = -\mathbf{p}_I = (-p_I, 0) \tag{3.1a}$$

$$\mathbf{p}(B^+) = \frac{m(B^+)}{m(BC^{2+})}\mathbf{p}_I + \mathbf{p}_{II} = \left(\frac{m(B^+)}{m(BC^{2+})}p_I + p_{II}\cos\phi, p_{II}\sin\phi\right) \tag{3.1b}$$

$$\mathbf{p}(C^+) = \frac{m(C^+)}{m(BC^{2+})}\mathbf{p}_I + \mathbf{p}_{II} = \left(\frac{m(C^+)}{m(BC^{2+})}p_I - p_{II}\cos\phi, -p_{II}\sin\phi\right) \tag{3.1c}$$

where m is the mass of the corresponding ion and $\mathbf{p}_I$ and $\mathbf{p}_{II}$ are the momenta imposed on the fragments in the first and the second step (see Figure 8). The momentum angle between $\mathbf{p}_I$ and $\mathbf{p}_{II}$ is denoted as ϕ. The kinetic energy released in each step can be calculated as $E_I = [m(A^+) + m(BC^{2+})]p_I^2/[2m(A^+)m(BC^{2+})]$ and $E_{II} = [m(B^+) + m(C^+)]\ p_{II}^2/[2m(B^+)m(C^+)]$, respectively.

Trial-and-error fittings to the experimental data were performed based on this free-rotor model using p_I and p_{II}, the absolute values of $\mathbf{p}_I$ and $\mathbf{p}_{II}$, as adjustable parameters. The results of the fitting, shown by the red solid lines, reproduced well the observed distributions in Figure 5 and parts c and d of Figure 6. It is noted that the distribution along the solid line is almost uniform, which indicates that the lifetimes of the intermediate precursor ions are sufficiently longer than their rotational periods which would be of the order of 1 ps or less depending on the extent of the rotational excitation upon fragmentation.

The free-rotor model is applied to the other three-body Coulomb explosion pathways and reproduces well the observed momentum correlations as plotted in Figures 6 and 7, showing that all of these Coulomb explosion dynamics proceed mainly in a sequential manner. For the analysis of the pathway 3h forming three identical fragment ions, we employed the Dalitz

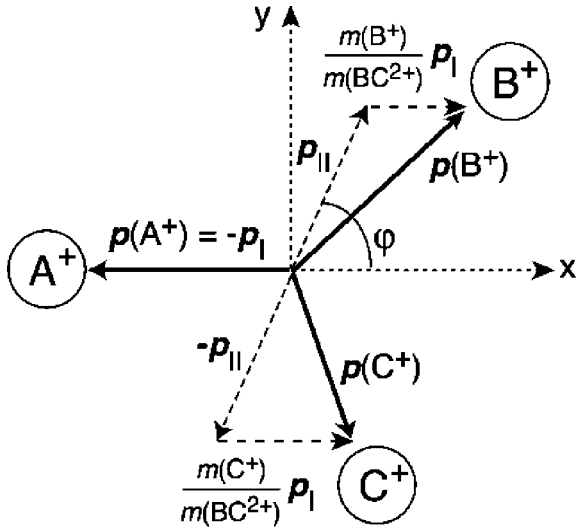

Figure 8. Newton diagram for the sequential three-body Coulomb explosion, $ABC^{3+} \rightarrow A^+ + BC^{2+} \rightarrow A^+ + B^+ + C^+$, based on the free rotor model.[21]

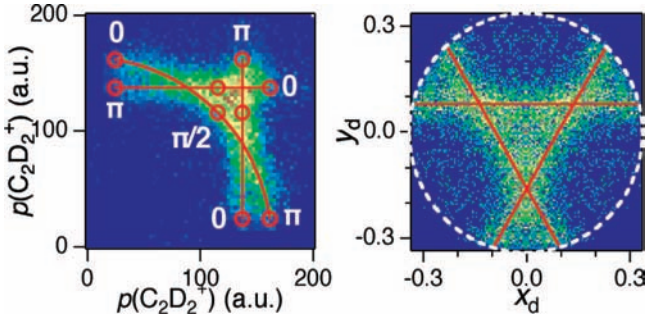

Figure 9. (left) Two-dimensional momentum correlation map, and (right) the Dalitz plot for the symmetrical three-body Coulomb explosion 3*h*, $C_6D_6^{3+} \rightarrow C_2D_2^+ + C_2D_2^+ + C_2D_2^+$ in the momentum space. The circle indicated in part b represents the boundary of momentum conservation condition. The results of simulations based on the free-rotor model for the sequential three-body explosion are shown by the red solid lines. The momentum angles between $\mathbf{p}_I$ and $\mathbf{p}_{II}$ (see text) are indicated with circles on the simulated lines.

plot analysis, developed originally to describe the three-body reactions in elementary particle physics[32] and applied recently to the Coulomb explosion processes in intense laser fields.[23]

In a Dalitz plot, the fragment kinetic energies normalized by the total kinetic energy release, $\varepsilon_i = E_i/E_{kin}$ ($i = 1 - 3$), are plotted in the Cartesian coordinate system $(x_d, y_d) = ((\varepsilon_1 - \varepsilon_2)/\sqrt{3}, \varepsilon_3 - 1/3)$. The Dalitz plot obtained for the pathway 3h is shown in Figure 9 together with the $p(C_2D_2^+) - p(C_2D_2^+)$ two-dimensional map. While the observed distribution is congested in the conventional momentum map (Figure 9, left), the corresponding Dalitz plot clearly exhibits three straight lines, forming a triangle pattern due to the 3-fold symmetry. Since a straight line distribution along the x_d coodinate appears in the Dalitz plot when the fragment kinetic energy ε_3 is constant irrespective of the others, ε_1 and ε_2, the observed distribution clearly shows that the fragmentation proceeds as $C_6D_6^{3+} \rightarrow C_2D_2^+ + C_4D_4^{2+} \rightarrow C_2D_2^+ + C_2D_2^+ + C_2D_2^+$, as discussed above. The results of the free-rotor simulation are plotted as the solid red curves in Figure 9.

The momentum correlations clearly show that all of the three-body Coulomb explosion pathways observed in the present study proceed primarily in a stepwise manner. In other words, the three-body Coulomb explosion of the benzene trication proceeds via two successive two-body Coulomb explosion processes. The identified sequential three-body explosion pathways are summarized in Table 3 together with the determined momentum parameters, p_I and p_{II}. For clarity, the two-body pathways identified in the present study (see Table 1) are listed again in Table 3.

D. Fragmentation Dynamics of the Benzene Trication, $C_6D_6^{3+}$. Table 3 clearly shows that all of the Coulomb explosion process from $C_6D_6^{3+}$ proceed via the formation of doubly charged precursor ions. The two-body Coulomb explosion pathways of the benzene trication have been discussed in recent theoretical studies.[13] The calculated potential energy surface for the electronic ground state of $C_6D_6^{3+}$ shows the routes toward the observed two-body fragmentation from the cyclic, benzene-like structure. With the exception of the direct deprotonation process, $C_6H_6^{3+} \rightarrow H^+ + C_6H_5^{2+}$, all the two-body processes are associated with multiple hydrogen migration and a rearrangement of the carbon chain. For example, the opening of the benzene ring proceeds with the double 1,2-hydrogen migration to the terminal carbon sites via a transition state located 1.66 eV above the initial state. The ring-opening then leads to the fragmentation to $CH_3^+ + C_5H_3^{2+}$, $C_2H_3^+ + C_4H_3^{2+}$, (c-)$C_3H_3^+ + C_3H_3^{2+}$, $C_4H_2^+ + C_2H_4^{2+}$ [13] and to $C_2H_2^+ + C_4H_4^{2+}$.[13] Another pathway, proceeding via the formation of five-members ring instead of the ring opening, is also open to form the cyclobutadiene dication c-$C_4H_4^{2+}$ together with $C_2H_2^+$.[13]

The kinetic energy release for the first two-body explosion process, E_I, is calculated for each pathway from the corresponding momentum value, p_I. Table 3 shows that the E_I values obtained from the different final pathways agree well each other for a given two-body explosion pathway from $C_6D_6^{3+}$. For example, the E_I values obtained for five different sequential pathways (3a″, d″, e″, g, h) all fall in the range between 7.3−7.5 eV, indicating that the first two-body explosion, $C_6D_6^{3+} \rightarrow C_2D_2^+ + C_4D_4^{2+}$, of these five pathways proceeds via a common transition state.

The obtained values of E_I can be compared with theoretical values, ΔE, calculated from the energy differences between the product states and the final potential barriers to the Coulomb explosion (referred to as "Coulomb repulsion transition states")[13] in Table 3. The overall agreement with the experimental E_I values indicates that (i) the first two-body explosion predominantly proceeds in the electronic ground state, (ii) the internal energy imparted to the parent ion upon the initial ionization step is distributed over many vibrational modes perpendicular to the Coulomb explosion reaction coordinate, and (iii) the Coulomb repulsion potential is mostly converted to the translational energies of the two fragments. It is noted that two significantly different values, $\Delta E = 4.9$ and 6.8 eV, are reported for the linear $C_3H_3^+ + C_3H_3^{2+}$ and cyclo-$C_3H_3^+ + C_3H_3^{2+}$ pathways, respectively. This may explain the difference in E_I observed for the two-body (2e) and three-body (3c″) components in the $C_3D_3^+ + C_3D_3^{2+}$ pathway. While the three-body pathway 3c″ gives $E_I = 6.4$ eV, a smaller value, 5.9 eV, is obtained from the two-body pathway 2e.

A closer inspection of Table 3 reveals that in some cases the observed E_I values are smaller than the theoretical predictions by 0.5−1.0 eV, showing that the Coulomb potential can also be transferred to the internal energy of the fragment ions. It should be noted that such pathways, $D^+ + C_6D_5^{2+}$ and $C_2D_2^+ + C_4D_4^{2+}$, exhibit heavy fragmentation from the fragment dication, $C_6D_5^{2+}$ and $C_4D_4^{2+}$, resulting in the sequential three-body Coulomb explosion processes. The fragmentation from the $C_4H_4^{2+}$ dication is discussed in ref 13. The transition state to

TABLE 3: Summary of Coulomb Explosion Pathways from $C_6D_6^{3+}$ in 9-fs Intense Laser Fields (1×10^{15} W/cm^2) Identified by the Double and Triple Ion-Coincidence Momentum Imaging Technique (Labels with Primes Indicate Pathways with Identical Products which Originate in Different Sequential Processes)

parent	step I	step II		N_{coinc} [a,b]	p_I (au.)	p_{II} (au.)	E_I (eV)	ΔE [c] (eV)	E_{II} (eV)
$C_6D_6^{3+}$	→ $D^+ + C_6D_5^{2+}$	→ $D^+ + C_2D_2^+ + C_4D_3^+$	3a′	1770(42)	39(1)	95(1)	5.8(3)	6.3	3.7(1)
		→ $D^+ + C_2D_3^+ + C_4D_2^+$	3b′	976(31)	39(1)	99(1)	5.8(3)	6.3	3.8(1)
		→ $D^+ + C_3D_2^+ + C_3D_3^+$	3c′	2246(47)	39(1)	109(1)	5.8(3)	6.3	4.3(1)
	→ $CD^+ + C_5D_5^{2+}$	→ $CD^+ + C_2D_2^+ + C_3D_3^+$	3d′	264(16)	107(1)	100(1)	7.3(1)	6.8	4.4(1)
	→ $CD_2^+ + C_5D_4^{2+}$		2a	*258(16)*		---	7.0(1)	5.8	---
		→ $CD_2^+ + C_2D_2^+ + C_3D_2^+$	3e′	981(31)	109(1)	99(1)	6.8(1)	5.8	4.0(1)
		→ $CD_2^+ + C_2D_3^+ + C_3D^+$	3f′	385(20)	110(1)	92(1)	7.0(1)	5.8	3.9(1)
	→ $CD_3^+ + C_5D_3^{2+}$		2b	*1054(32)*		---	6.8(1)	7.0	---
	→ $C_2D_2^+ + C_4D_4^{2+}$	→ $C_2D_2^+ + D^+ + C_4D_3^+$	3a″	422(21)	137(1)	28(1)	7.5(1)	8.3, 8.5	3.0(1)
		→ $C_2D_2^+ + CD^+ + C_3D_3^+$	3d″	176(13)	137(1)	80(2)	7.5(1)	8.3, 8.5	4.5(1)
		→ $C_2D_2^+ + CD_2^+ + C_3D_2^+$	3e″	981(31)	136(1)	77(1)	7.4(1)	8.3, 8.5	4.2(1)
		→ $C_2D_2^+ + CD_3^+ + C_3D^+$	3g	4190(65)	135(1)	78(1)	7.3(1)	8.3, 8.5	3.7(1)
		→ $C_2D_2^+ + C_2D_2^+ + C_2D_2^+$	3h	2822(53)	137(1)	93(1)	7.5(1)	8.3, 8.5	4.6(1)
	→ $C_2D_3^+ + C_4D_3^{2+}$		2c	*13795(117)*		---	6.4(1)	6.4	---
		→ $C_2D_3^+ + D^+ + C_4D_2^+$	3b″	976(31)	132(1)	28(1)	6.7(1)	6.4	3.0(1)
		→ $C_2D_3^+ + CD_2^+ + C_3D^+$	3f″	1540(39)	133(1)	74(1)	6.8(1)	6.4	3.6(1)
	→ $C_3D_2^+ + C_3D_4^{2+}$		2d	*2109(46)*		---	6.3(1)	5.3	---
	→ $C_3D_3^+ + C_3D_3^{2+}$		2e	*8719(93)*		---	5.9(1)	4.9, 6.8	---
		→ $C_3D_3^+ + D^+ + C_3D_2^+$	3c″	1497(39)	134(1)	28(1)	6.4(1)	4.9, 6.8	3.1(1)

[a] Number of events estimated for each pathway from (i) the number of events for the corresponding three-body pathway and (ii) the branching ratio evaluated from the number density at $\phi = \pi/2$. The experimental uncertainty is estimated as $\sqrt{N_{coinc}}$. [b] Numbers in italics are from Table 1 for the two-body pathways, which should be multiplied by 0.6 (the MCP aperture ratio) to be compared with those for the three-body pathways. [c] Theoretical estimates based on the *ab initio* potential energy surface[13] (see text).

the $C_2H_2^+ + C_2H_2^+$ dissociation is located 6.97 eV above the cyclo-$C_4H_4^{2+}$ state, showing that a large amount of internal energy ≳6 eV needs to be deposited into the $C_4H_4^{2+}$ moiety in $C_6H_6^{3+}$ prior to the first step dissociation to $C_2H_2^+ + C_4H_4^{2+}$. The E_{II} value estimated as described above from the theoretical potential energy surface is 4.65 eV, which is again in good agreement with the observed results (4.6 eV).

The Rice−Ramsperger−Kassel−Marcus (RRKM) calculations performed with the ground potential energy surface[13] show that the $C_3H_3^+ + C_3H_3^{2+}$ (81.5%) and $C_2H_3^+ + C_4H_3^{2+}$ (13.2%) pathways are dominant at the initial internal energy of 4.76 eV, with minor contributions from the other pathways, e.g., $C_2H_2^+ + c\text{-}C_4H_4^{2+}$ (0.49%). The experimental branching ratio of the first two-body Coulomb explosion pathways may be estimated from the number of events for each explosion pathway.[34] Table 3 shows the number of events for each explosion pathway observed in the present study, calculated from (i) the number of total events of the corresponding three-body pathway and (ii) the branching ratio of the contributing sequential pathways, evaluated from the number density at $\phi = \pi/2$ to avoid the overlap of different components (see Figures 6, 7, 9).

The numbers of events thus obtained show clearly that there is no strong propensity in the first two-body Coulomb explosion pathways. Interestingly, significantly large contributions are observed for the "minor" pathways, e.g., $C_2D_2^+ + C_4D_4^{2+}$ and $D^+ + C_6D_5^{2+}$, with large barriers for reaction (2.3−2.7 eV) whose branching fractions of these pathways being 5.24 and 2.24%, respectively, even at a significantly higher initial internal energy (9.53 eV).[13] It is also noted that two pathways expected from the theoretical calculations,[13] $C_2D_4^+ + C_4D_2^{2+}$ and $C_4D_2^+ + C_2D_4^{2+}$, are not identified. These deviations from the RRKM predictions show that the observed fragmentation of $C_6D_6^{3+}$ is not fully statistical and indicate that the decomposition process is fast compared to the intramolecular vibrational energy redistribution in $C_6D_6^{3+}$. The deformation of the potential energy surface in intense laser fields may play an additional role: A recent theoretical study[14] predicted a significant lowering of the potential barrier (∼2.4 eV) for the deprotonation process from the benzene trication at a field intensity of 3×10^{14} W/cm^2. Another possible source of the deviation may be the enhanced ionization,[1] which can be persistent in the few-cycle laser fields due to the rapid nuclear motion of a deuterium atom in the multiple ionization process.[35]

IV. Summary

Multiple Coulomb explosion processes of the deuterated benzene trication, $C_6D_6^{3+}$, formed in 9-fs intense laser fields (1×10^{15} W/cm^2) were studied by ion-coincidence momentum imaging. Five two-body and eight three-body Coulomb explosion pathways were identified. The analysis of the fragment momentum correlation revealed that all of the observed three-body explosion processes proceed sequentially via the formation of molecular dications $C_mD_n^{2+}$, with $(m,n) = (6,5)$, $(5,5)$, $(5,4)$, $(4,4)$, $(4,3)$, and $(3,3)$ as precursors. The branching ratios of the observed Coulomb explosion pathways, estimated from the number of the corresponding coincidence events, largely deviate from the previous RRKM prediction, showing that the dissociation processes are not fully statistical. The experimental results obtained in the present study using few-cycle laser pulse should serve as a reference for understanding the dynamics of aromatic molecules in intense laser fields. The role of the intense laser fields in the fragmentation processes, such as the deformation of the potential energy surface, the resonant[7,33] or nonresonant[10] coupling between the electronic states or electron rescattering,[17] would become clearer by comparison with the experiments performed with longer intense laser pulses, which allows the nuclear motion under the interaction with the laser fields.

Acknowledgment. R.D.T. and V.Z. would like to acknowledge support from STINT for the visit to IMS.

References and Notes

(1) Posthumus, J. H. *Rep. Prog. Phys.* **2004**, *67*, 623.
(2) Hertel, I. V.; Radloff, W. *Rep. Prog. Phys.* **2006**, *69*, 1897.

(3) Dewitt, M. J.; Levis, R. J. *J. Chem. Phys.* **1995**, *102*, 8670.

(4) Ledingham, K. W. D.; Smith, D. J.; Singhal, R. P.; McCanny, T.; Graham, P.; Kilic, H. S.; Peng, W. X.; Langley, A. J.; Taday, P. F.; Kosmidis, C. *J. Phys. Chem.* **1999**, *103*, 2952.

(5) Talebpour, A.; Bandrauk, A. D.; Vijayalakshmi, K.; Chin, S. L. *J. Phys. B* **2000**, *33*, 4615.

(6) Shimizu, S.; Kou, J.; Kawato, S.; Shimizu, K.; Sakabe, S.; Nakashima, N. *Chem. Phys. Lett.* **2000**, *317*, 609.

(7) Itakura, R.; Watanabe, J.; Hishikawa, A.; Yamanouchi, K. *J. Chem. Phys.* **2001**, *114*, 5598.

(8) Tasker, A. D.; Robson, L.; Ledingham, K. W. D.; McCanny, T.; Hankin, S. M.; McKenna, P.; Kosmidis, C.; Jaroszynski, D. A.; Jones, D. R. *J. Phys. Chem.* **2002**, *106*, 4005.

(9) Rajgara, F. A.; Krishnamurthy, M.; Mathur, D. *Phys. Rev. A* **2003**, *68*, 023407.

(10) Markevitch, A. N.; Romanov, D. A.; Smith, S. M.; Levis, R. J. *Phys. Rev. Lett.* **2004**, *92*, 063001.

(11) Markevitch, A. N.; Romanov, D. A.; Smith, S. M.; Levis, R. J. *Phys. Rev. Lett.* **2006**, *96*, 163002.

(12) Yatsuhashi, T.; Murakami, M.; Nakashima, N. *J. Chem. Phys.* **2007**, *126*, 194316.

(13) Zyubina, T. S.; Kim, G.-S.; Mebel, A. M.; Lin, S. H.; Bandrauk, A. D. *J. Theor. Comput. Chem.* **2003**, *2*, 205.

(14) Mebel, A. M.; Zyubina, T. S.; Dyakov, Y. A.; Bandrauk, A. D.; Lin, S. H. *Int. J. Quantum Chem.* **2005**, *102*, 506.

(15) Anand, S.; Schlegel, H. B. *J. Phys. Chem. A* **2005**, *109*, 11551.

(16) Castillejo, M.; Couris, S.; Koudoumas, E.; Martin, M. *Chem. Phys. Lett.* **1998**, *289*, 303.

(17) Bhardwaj, V. R.; Rayner, D. M.; Villeneuve, D. M.; Corkum, P. B. *Phys. Rev. Lett.* **2001**, *87*, 253001.

(18) Hasegawa, H.; Hishikawa, A.; Yamanouchi, K. *Chem. Phys. Lett.* **2001**, *349*, 57.

(19) Richardson, P. J.; Eland, J. H. D.; Lablanquie, P. *Org. Mass Spectrom.* **1986**, *21*, 289.

(20) Rajgara, F. A.; Krishnamurthy, M.; Mathur, D.; Nishide, T.; Shiromaru, H.; Kobayashi, N. *J. Phys. B* **2004**, *37*, 1699.

(21) Hishikawa, A.; Hasegawa, H.; Yamanouchi, K. *Chem. Phys. Lett.* **2002**, *361*, 245.

(22) Hishikawa, A.; Takahashi, E. J.; Matsuda, A. *Phys. Rev. Lett.* **2006**, *97*, 243002.

(23) Matsuda, A.; Takahashi, E. J.; Hishikawa, A. *J. Chem. Phys.* **2007**, *127*, 114318.

(24) Eppink, A. T. J. B.; Parker, D. H. *Rev. Sci. Instrum.* **1997**, *68*, 3477.

(25) Fraser, G. T. *Int. J. Mass Spectrom.* **2002**, *215*, 13.

(26) Krems, M.; Zirbel, J.; Thomason, M.; DuBois, R. D. *Rev. Sci. Instrum.* **2005**, *76*, 093305.

(27) Ullrich, J.; Moshammer, R.; Dorn, A.; Dörner, R.; Schmidt, L. P. H.; Schmidt-Böcking, H. *Rep. Prog. Phys.* **2003**, *66*, 1463.

(28) Zare, R. N. *Mol. Photochem.* **1972**, *4*, 1. Here θ and $P_2(x)$ represent the angle from the direction of the laser polarization vector and the Legendre polynomial of the second order, respectively. .

(29) Hishikawa, A.; Matsuda, A.; Takahashi, E. J.; Fushitani, M. *J. Chem. Phys.* **2008**, *128*, 084302.

(30) Hishikawa, A.; Hasegawa, H.; Yamanouchi, K. *Chem. Phys. Lett.* **2004**, *388*, 1.

(31) Liu, P.; Okino, T.; Furukawa, Y.; Ichikawa, T.; Itakura, R.; Hoshina, K.; Yamanouchi, K.; Nakano, H. *Chem. Phys. Lett.* **2006**, *423*, 187.

(32) Dalitz, R. H. *Philos. Mag.* **1953**, *44*, 1068.

(33) Harada, H.; Shimizu, S.; Yatsuhashi, T.; Sakabe, S.; Izawa, T.; Nakashima, N. *Chem. Phys. Lett.* **2001**, *342*, 563.

(34) Note that the effect of small variation of ion detection efficiency on relative yields would be less significant in multiple coincidence measurements than in single ion detection, since overall efficiency of a given explosion pathway is determined by the product of the detection efficiencies of the relevant fragment ions.

(35) Légaré, F.; Litvinyuk, I. V.; Dooley, P. W.; Quere, F.; Bandrauk, A. D.; Villeneuve, D.; Corkum, P. B. *Phys. Rev. Lett.* **2003**, *91*, 093002.

JP806466X